CELL BIOLOGY

Golgi-derived PI(4)P-containing vesicles drive late steps of mitochondrial division

Shun Nagashima[1], Luis-Carlos Tábara[1]*, Lisa Tilokani[1]*, Vincent Paupe[1], Hanish Anand[1], Joe H. Pogson[2], Rodolfo Zunino[2], Heidi M. McBride[2]†, Julien Prudent[1]†

Mitochondrial plasticity is a key regulator of cell fate decisions. Mitochondrial division involves Dynamin-related protein-1 (Drp1) oligomerization, which constricts membranes at endoplasmic reticulum (ER) contact sites. The mechanisms driving the final steps of mitochondrial division are still unclear. Here, we found that microdomains of phosphatidylinositol 4-phosphate [PI(4)P] on trans-Golgi network (TGN) vesicles were recruited to mitochondria–ER contact sites and could drive mitochondrial division downstream of Drp1. The loss of the small guanosine triphosphatase ADP-ribosylation factor 1 (Arf1) or its effector, phosphatidylinositol 4-kinase IIIβ [PI(4)KIIIβ], in different mammalian cell lines prevented PI(4)P generation and led to a hyperfused and branched mitochondrial network marked with extended mitochondrial constriction sites. Thus, recruitment of TGN-PI(4)P–containing vesicles at mitochondria–ER contact sites may trigger final events leading to mitochondrial scission.

Mitochondrial division is initiated at sites where the endoplasmic reticulum (ER) contacts mitochondria, which marks the site of constriction and subsequent recruitment of the large guanosine triphosphatase (GTPase) Dynamin-related protein-1 (Drp1) (*1*). At these sites, Drp1 oligomerization further enhances mitochondrial constriction driven by GTP hydrolysis (*2*). It has been suggested that the GTPase Dynamin 2 (Dnm2) is required downstream of Drp1-mediated constriction to terminate membrane scission (*3*); however, its precise contribution and the molecular details of late events are currently unclear (*4*, *5*). A growing body of evidence supports the role of other factors regulating mitochondrial division, including phospholipids, calcium, and lysosomes (*6*). Furthermore, a recent study revealed that loss of the small GTPase ADP-ribosylation factor 1 (Arf1) led to alterations in mitochondrial morphology with hyperfusion in *Caenorhabditis elegans* (*7*). GTP-bound Arf1 is recruited primarily to the Golgi apparatus, where it is canonically known for its role in the generation of COP1-coated vesicles. GTP-specific effector proteins of Arf1 include phosphatidylinositol 4-kinase-III-β [PI(4)KIIIβ], which mediates the phosphorylation of phosphatidylinositol to generate phosphatidylinositol 4-phosphate [PI(4)P] (*8*). This generates lipid microdomains enriched for PI(4)P that are required for membrane-remodeling events (*9*–*12*). Given the primary role for these enzymes in membrane dynamics (*7*, *13*), we investigated the mechanisms that underlie the contribution of PI(4)P pools in the regulation of mitochondrial morphology.

Silencing of both Arf1 and PI(4)KIIIβ led to mitochondrial hyperfusion in HeLa cells (Fig. 1, A to D). In contrast to Drp1-silenced cells, loss of PI(4)KIIIβ and Arf1 induced mitochondrial elongation and mitochondrial branching, leading to a highly interconnected network and an increase of mitochondrial intersections called junctions (Fig. 1E). These results were confirmed in two other mammalian cell lines, Cos-7 and U2OS (fig. S1, A to K). We further quantified mitochondrial interconnectivity using a photoactivatable GFP probe targeted to the mitochondrial matrix (OCT-PAGFP) (*14*) (Fig. 1, F and G). Mitochondrial hyperfusion induced by PI(4)KIIIβ silencing was rescued upon reexpression of the bovine wild-type (WT) PI(4)KIIIβ (PI4K-HA), but not with the kinase-dead mutant (PI4K-KD-HA) (*15*) (Fig. 1, H and I, and fig. S1, L and M). Treatment of HeLa or Cos-7 cells with the selective PI(4)KIIIβ inhibitor PIK93 also resulted in mitochondrial hyperfusion and branching (fig. S2). In addition, among the PI(4)K family, only PI(4)KIIβ silencing induced mild mitochondrial hyperfusion in HeLa cells (fig. S3A-G), but not in Cos-7 cells (fig. S3H-N), which may be coincident with a cell-type–specific decrease of Drp1 and PI(4)KIIIβ protein levels upon silencing (fig. S3F). Finally, cells silenced for ceramide transfer protein (CERT), another Arf1 effector, did not lead to mitochondrial hyperfusion (fig. S4). Thus, both the kinase activity of the specific effector PI(4)KIIIβ and the GTPase Arf1 are required to modulate mitochondrial dynamics.

In transmission electron microscopy (TEM), PI(4)KIIIβ- and Arf1-silenced cells displayed exaggerated mitochondrial hyperfusion and branching (Fig. 2, A to D, and fig. S5A). We observed an accumulation of unusual mitochondrial-hyperconstricted sites in cells lacking either Arf1 or PI(4)KIIIβ (Fig. 2, E to G, and fig. S5, B and C). These sites were characterized by a long and narrow neck, where the inner membrane was observed running parallel with the constricted outer membrane (Fig. 2, A, E, and F, and fig. S5B). In addition, the ER was in close apposition along these constricted sites (Fig. 2G), suggesting that mitochondria–ER contacts (MERCs) were maintained. A similar level of mitochondrial hyperconstriction has been reported in cells silenced with Dnm2 (*3*), where it has been suggested that this dynamin may act downstream of Drp1 to drive fission. However, silencing Dnm2 in U2OS and HeLa cells failed to recapitulate the mitochondrial hyperfusion and branching phenotype induced by the loss of PI(4)P pools (fig. S6), as recently reported (*4*, *5*), suggesting that Arf1 and PI(4)KIIIβ may not be required for Dnm2 recruitment.

Loss of Arf1 in yeast results in an accumulation of the fusion GTPase Fzo1 at mitochondria and an alteration in mitochondrial morphology (*7*). However, we found no major changes in the levels of the main pro-fission and pro-fusion regulators after 48 or 72 hours of silencing for Arf1 or PI(4)KIIIβ, respectively, in HeLa (Fig. 2H), Cos-7 (fig. S5D), and U2OS (fig. S5E) cells. Although Arf1 silencing for 3 days led to ER morphology aberrations and increased levels of cell death (fig. S7), we still did not observe changes in the main fission and fusion regulator levels (fig. S7D). Immunofluorescence analysis of endogenous Mfn1 and Mfn2 in PI(4)KIIIβ- and Arf1-silenced HeLa cells also did not reveal any aggregation or mislocalization (fig. S5, F and G). In addition, subcellular distribution analyses of Drp1 revealed no mitochondrial recruitment defects (Fig. 2, I to K) and the presence of Drp1 foci specifically at mitochondrial superconstrictions induced by loss of PI(4)KIIIβ in the human fibroblast line MCH64 (Fig. 2K). Furthermore, stimulated Drp1-dependent mitochondrial fission induced by mitochondrial-anchored protein ligase (MAPL) (*16*) overexpression (fig. S8, A and B) or by carbonyl cyanide chlorophenylhydrazone (CCCP) treatment (fig. S8, C and D) was significantly reduced in PI(4)KIIIβ- and Arf1-silenced cells. Silencing of the key component involved in stress-induced mitochondrial hyperfusion, SLP-2 (*17*), as well as the pro-fusion factors Mfn1 and Mfn2, also failed to reverse mitochondrial hyperfusion in PI(4)KIIIβ-silenced cells (fig. S9). Finally, compared with Drp1 silencing, which leads to drastic peroxisomal elongation (*18*, *19*), loss of Arf1 and PI(4)KIIIβ only induced a subtle peroxisomal elongation in HeLa cells, not in Cos-7 cells (fig. S10). Thus, these data potentially support a specific role for these enzymes in the regulation of mitochondrial fission downstream of Drp1 recruitment.

[1]Medical Research Council Mitochondrial Biology Unit, University of Cambridge, Cambridge Biomedical Campus, Cambridge CB2 0XY, UK. [2]Department of Neurology and Neurosurgery, McGill University, Montreal, Quebec H3B 2B4, Canada.
*These authors contributed equally to this work.
†Corresponding author. Email: heidi.mcbride@mcgill.ca (H.M.M.); julien.prudent@mrc-mbu.cam.ac.uk (J.P.)

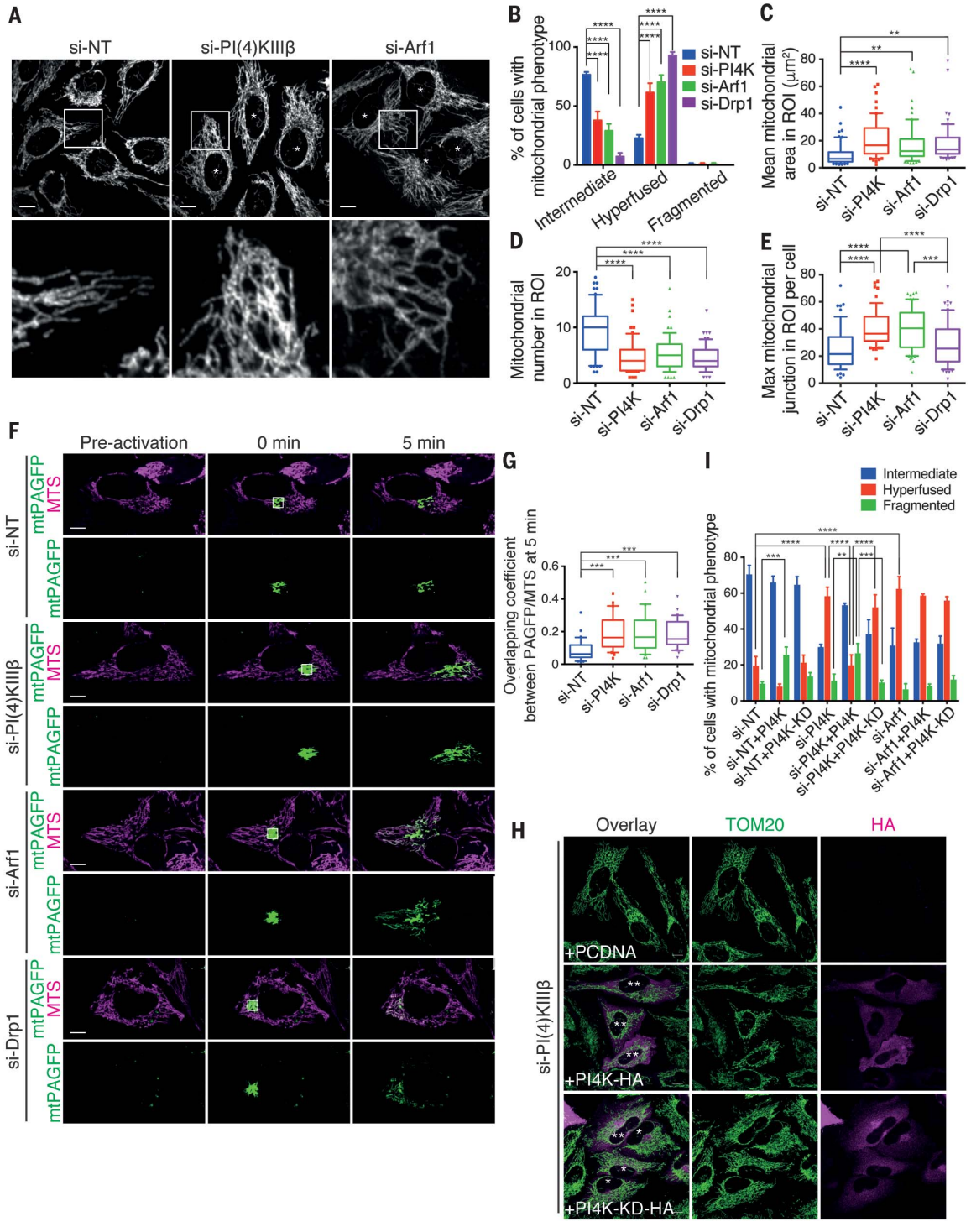

Fig. 1. Arf1 and PI(4)KIIIβ silencing lead to mitochondrial hyperfusion and branching. (**A**) Representative confocal images of mitochondrial morphology in HeLa cells treated with the indicated small interfering RNAs (siRNAs). Mitochondria were labeled using an anti-TOM20 antibody. Asterisks indicate cells with elongated and/or branched mitochondria. (**B**) Quantification of mitochondrial morphology from (A). (**C** to **E**) Mitochondrial morphology quantified for (C) mean mitochondrial area per mitochondrion, (D) mitochondrial number, and (E) mitochondrial branching measured by maximum mitochondrial junction number for each region of interest (ROI). (**F**) Live-cell imaging of HeLa cells treated with indicated siRNAs overexpressing the ornithine carbamoyltransferase (OCT)-photoactivatable GFP (mt-PAGFP) probe and the mitochondrial marker MTS-Scarlet. (**G**) Quantification of the OCT-PAGFP probe diffusion over a 5-min period from (F) using the overlapping Mander's coefficient. (**H**) Representative confocal images of mitochondrial morphology in HeLa cells silenced with PI(4)KIIIβ siRNA and transiently overexpressing empty vector (vehicle), WT-PI(4)KIIIβ-HA (PI4K-HA), and kinase-dead mutant PI(4)KIIIβ-HA (PI4K-KD-HA). Shown are HA-positive transfected cells with elongated and/or branched mitochondria (*) and intermediate mitochondria (**). (**I**) Quantification of mitochondrial morphology from (H) and fig. S1L. All scale bars, 10 μm. All data are shown as mean ± SD of at least three independent experiments. For (B) and (I), two-way ANOVA and Tukey's multiple-comparisons test were used; for (C) to (E) and (G), ordinary one-way ANOVA and Tukey's multiple-comparisons test were used. See also table S1.

PI(4)KIIIβ mainly localized to the Golgi apparatus (fig. S11A) but PI(4)KIIIβ foci were also detected at ER-induced mitochondrial constriction sites (Fig. 3A and fig. S11B). Similar results were obtained for subcellular localization analysis of Arf1-GFP (fig. S11C). The presence of PI(4)KIIIβ and Arf1 at the MERC compartment was confirmed by subcellular fractionation experiment (Fig. 3B). We then performed live-cell imaging to determine whether Arf1-GFP was recruited to mitochondrial constriction sites before division (Fig. 3C and movies S1 and S2). About 71% of mitochondrial division events analyzed were marked with Arf1-GFP punctae before fission (Fig. 3D) and 77% of

division events showed the recruitment of these punctae at constriction sites after Drp1 recruitment (Fig. 3, E and F, and movie S3). Although Arf1-GFP foci were preferentially found on ER-induced mitochondrial constriction sites (fig. S11D and movies S4 and S5), Arf1-GFP foci were not localized at mitochondrial tip ends after division (Fig. 3, C and D, and movies S1 and S2) and they did not localize perfectly with ER markers (fig. S11D). This suggested that Arf1 was primarily recruited to the MERC during division from a ternary compartment. Previous work uncovered a role for lysosomes at sites of mitochondrial division (*20*), so we first explored whether Arf1-GFP foci may reflect these structures. However, whereas Arf1-GFP foci converged with lysosomes at fission sites, their recruitment was distinct from lysosomes (Fig. 3, G and H, and movie S6). Instead, we found that Arf1-GFP foci were recruited to constriction sites upon trans-Golgi network (TGN) vesicles (Fig. 3, I and J, and movie S7). Indeed, TGN46-mCherry vesicles were recruited to mitochondrial constriction just before division in 85% of fission events analyzed, which was correlated with a colocalization with Arf1-GFP punctae before and during this process in

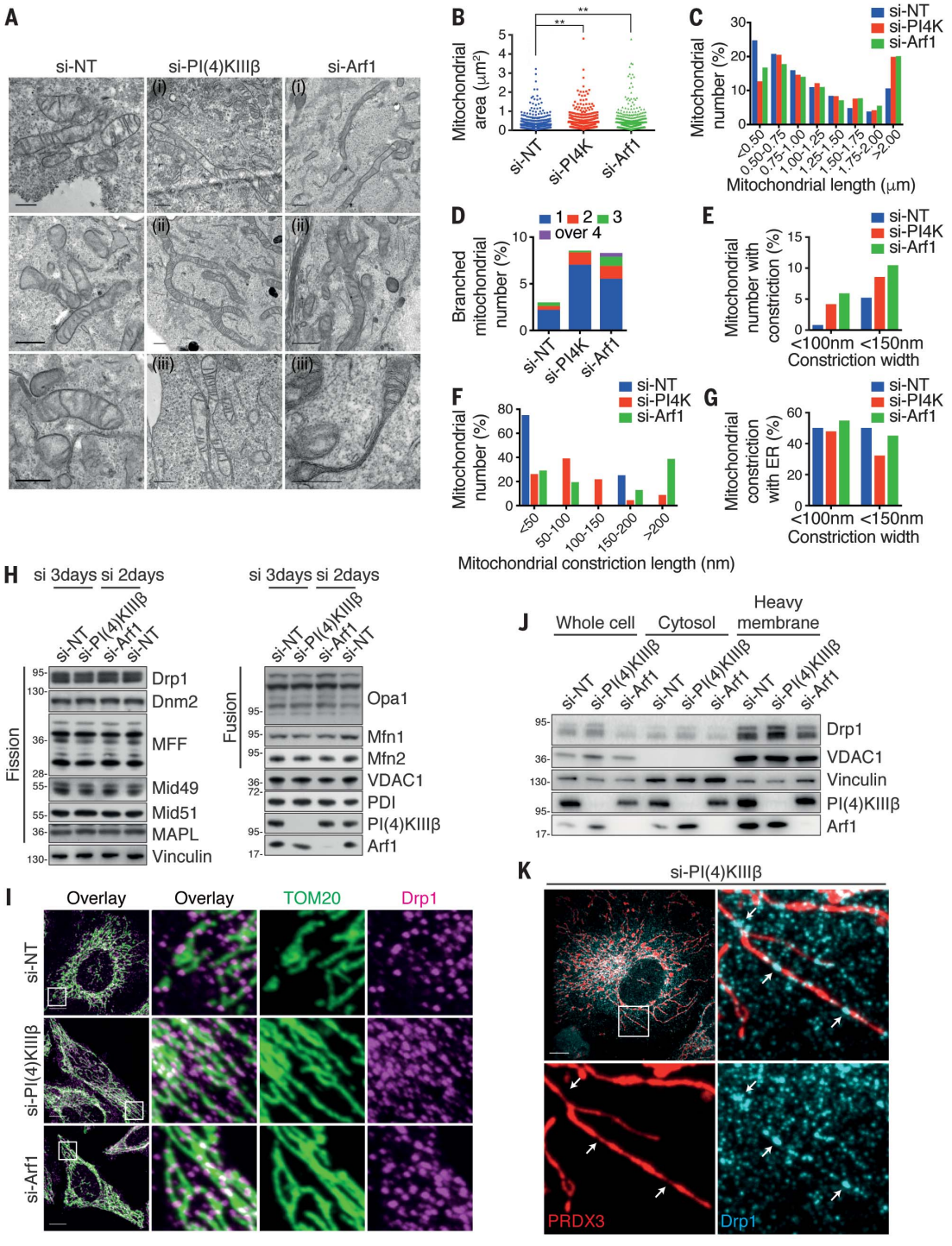

Fig. 2. Loss of Arf1 and PI(4)KIIIβ induces mitochondrial superconstriction sites and does not alter fusion and/or fission machinery. (**A**) Representative TEM images of HeLa cells treated with indicated siRNAs, showing (i) hyperfused mitochondria, (ii) branched mitochondria, and (iii) mitochondrial superconstriction sites with ER contacts. Scale bars, 500 nm. (**B** to **G**) Quantification of TEM images from (A) showing (B) mitochondrial area, (C) distribution of mitochondrial length, (D) percentage of branched mitochondria with indicated branch count, (E) percentage of mitochondria harboring mitochondrial superconstrictions, (F) distribution of mitochondrial superconstriction length (width <100 nm), and (G) percentage of mitochondrial superconstriction with ER contacts. (**H**) Levels of proteins relevant to mitochondrial fission (left panel) and fusion (right panel) from HeLa cells treated with the indicated siRNAs. (**I**) Representative confocal images of mitochondrial morphology and Drp1 localization in HeLa cells treated with the indicated siRNAs. Scale bars, 10 μm. (**J**) Subcellular fractionation analysis of Drp1 distribution in HeLa cells treated with the indicated siRNAs. Total cell lysates (whole cell) were fractionated into crude mitochondrial (heavy membrane) and cytosolic (cytosol) fractions. (**K**) Representative confocal images of Drp1 accumulating at mitochondrial superconstriction sites (white arrows) in human fibroblasts silenced for PI(4)KIIIβ. Scale bar, 10 μm. For (B), ordinary one-way ANOVA and Tukey's multiple-comparisons test were used in two independent experiments.

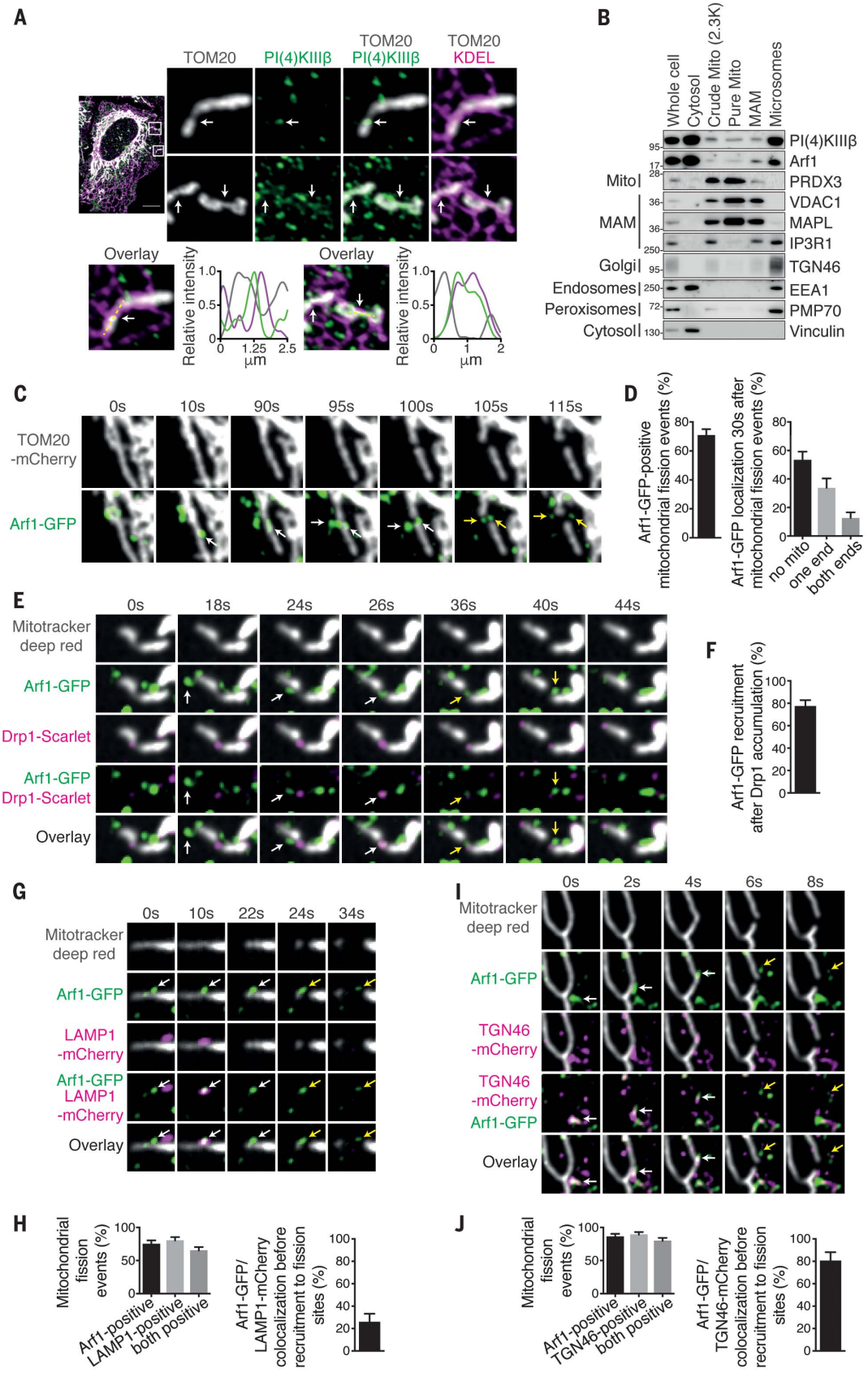

Fig. 3. PI(4)KIIIβ and Arf1 localized on TGN vesicles are recruited to mitochondrial constrictions and ER contacts before division. (**A**) Representative images of PI(4)KIIIβ punctae localization at mitochondrial constriction sites and ER contacts in HeLa cells (white arrows). Line-scan analysis of relative fluorescence intensity from the dashed line are shown. (**B**) PI(4)KIIIβ and Arf1 localization analysis by subcellular fractionation from HeLa cells. Total cell lysates (whole cell) were fractionated into cytosolic, heavy membrane (crude mito), purified mitochondrial (pure mito), mitochondria-associated membranes (MAM), and microsomal (microsomes) fractions. (**C**) Live-cell imaging of HeLa cells transiently expressing Arf1-GFP and TOM20-mCherry. (**D**) Quantification of mitochondrial fission events marked by Arf1-GFP before division (left panel) and Arf1-GFP dynamics on mitochondria after division (right panel). (**E**) Live-cell imaging of HeLa cells transiently expressing Arf1-GFP and Drp1-Scarlet with mitochondria labeled using MitoTracker deep red. (**F**) Quantification of mitochondrial fission events marked by Arf1-GFP downstream of Drp1-Scarlet recruitment. (**G**) Live-cell imaging of HeLa cells transiently expressing Arf1-GFP and LAMP1-mCherry with mitochondria labeled using MitoTracker deep red. (**H**) Quantification of mitochondrial fission events marked by Arf1-GFP, LAMP1-mCherry, or double Arf1-GFP/LAMP1-mCherry before division (left panel) and Arf1-GFP/LAMP1-mCherry dynamics before recruitment to division sites (right panel). (**I**) Live-cell imaging of HeLa cells transiently expressing Arf1-GFP and TGN46-mCherry with mitochondria labeled using MitoTracker deep red. (**J**) Quantification of mitochondrial fission events marked by Arf1-GFP, TGN46-mCherry, or double Arf1-GFP/TGN46-mCherry before division (left panel) and Arf1-GFP/TGN46-mCherry dynamics before recruitment to division sites (right panel). In (C), (E), (G), and (I), white and yellow arrows indicate Arf1-GFP puncta before and after a fission event, respectively. All scale bars, 10 μm. All data are shown as mean ± SEM of at least three independent experiments.

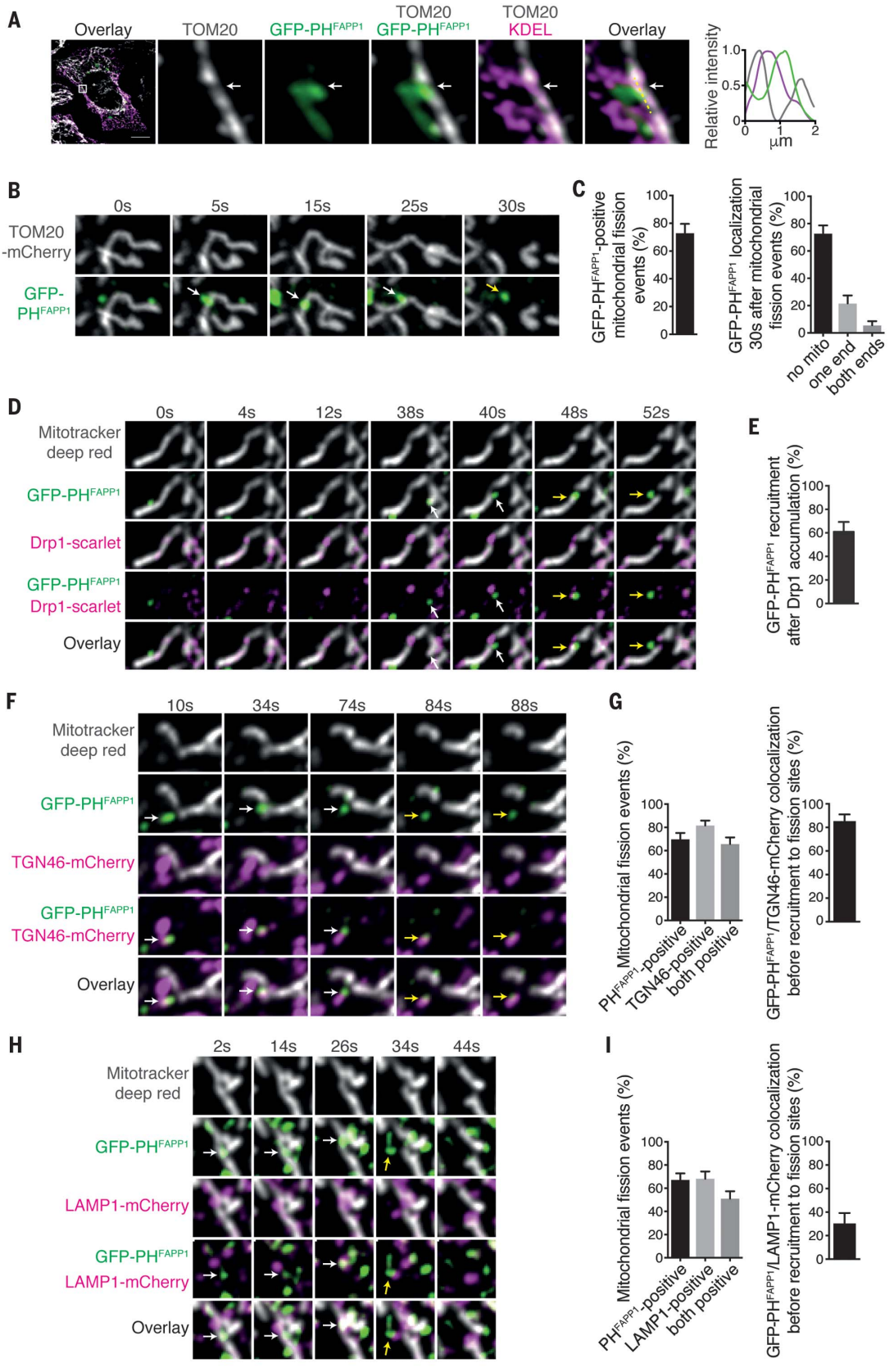

Fig. 4. Arf1- and PI(4)KIIIβ-dependent PI(4)P formation on TGN vesicles at mitochondrial constrictions and ER contacts drive mitochondrial fission. (**A**) Representative confocal images of HeLa cells transfected with GFP-PH^{FAPP1} showing GFP-PH^{FAPP1} at mitochondrial constriction sites and ER contact localization (white arrows). Line-scan analysis of relative fluorescence intensity from the dashed line is shown. (**B**) Live-cell imaging of HeLa cells transiently expressing GFP-PH^{FAPP1} and TOM20-mCherry. (**C**) Quantification of mitochondrial fission events marked by GFP-PH^{FAPP1} before division (left panel) and 30 s after division (right panel). (**D**) Live-cell imaging of HeLa cells transiently expressing GFP-PH^{FAPP1} and Drp1-Scarlet with mitochondria labeled using MitoTracker deep red. (**E**) Quantification of mitochondrial fission events marked by GFP-PH^{FAPP1} downstream of mitochondrial Drp1-Scarlet recruitment. (**F**) Live-cell imaging of HeLa cells transiently expressing GFP-PH^{FAPP1} and TGN46-mCherry with mitochondria labeled using MitoTracker deep red. (**G**) Quantification of mitochondrial fission events marked by GFP-PH^{FAPP1}, TGN46-mCherry, or double GFP-PH^{FAPP1}/TGN46-mCherry before division (left panel) and GFP-PH^{FAPP1}/TGN46-mCherry dynamics before recruitment to mitochondrial division sites (right panel). (**H**) Live-cell imaging of HeLa cells transiently expressing GFP-PH^{FAPP1} and LAMP1-mCherry with mitochondria labeled using MitoTracker deep red. (**I**) Quantification of mitochondrial fission events marked by GFP-PH^{FAPP1}, LAMP1-mCherry, or double GFP-PH^{FAPP1}/LAMP1-mCherry before division (left panel) and GFP-PH^{FAPP1}/LAMP1-mCherry dynamics before recruitment to mitochondrial division sites (right panel). For (B), (D), (F), and (H), white and yellow arrows indicate GFP-PH^{FAPP1} puncta before and after a fission event, respectively. All scale bars, 10 μm. All data are shown as mean ± SEM of at least three independent experiments.

80% of division events (Fig. 3, I and J, and movie S7).

We confirmed the predominant Golgi localization for PI(4)P (fig. S12A) using the established probe GFP-PH^{FAPP1} (*21*), but we also observed PI(4)P enriched foci crossing ER-induced mitochondrial constriction sites (Fig. 4A) in an Arf1- and PI(4)KIIIβ-dependent manner (fig. S12, B and C). Loss of Drp1 also significantly decreased mitochondrial GFP-PH^{FAPP1} punctae, suggesting that Drp1 activity was required for the recruitment of TGN-derived PI(4)P vesicles (fig. S12, B and C). Video analysis revealed that pools of PI(4)P accumulated and extended toward mitochondria at sites of constriction (Fig. 4B and movies S8 and S9) in ~73% of division events analyzed (Fig. 4, B and C). Similar to Arf1-GFP, PI(4)P foci were recruited to MERCs downstream of Drp1 (Fig. 4, D and E; fig. S13; and movies S10 and S11) and remained on TGN46 vesicles throughout the fission event (Fig. 4, F and G, and movie S12). Moreover, we observed no colocalization with lysosomes that converged at the site of division (Fig. 4, H and I, and movie S13). These results were confirmed using an additional PI(4)P probe, mCherry-P4M, which recognizes PI(4)P pools in multiple endomembranes (*22*) (fig. S14 and movies S14 to S16). Finally, consistent with the assembly of the mitochondrial fission machinery and the coordination of PI(4)P accumulation, endogenous TGN46, PI(4)KIIIβ, and GFP-PH^{FAPP1} foci colocalized with endogenous Drp1 at ER-induced mitochondrial constrictions (fig. S15). Thus, Arf1 and PI(4)KIIIβ enable the accumulation of PI(4)P punctae on TGN vesicles, driving late steps of mitochondrial division.

Mitochondrial fission is a complex process that requires many factors, including the ER, which is involved in the early steps of organelle constriction (*1*, *23*), and the lysosomes, which were recently identified at division sites (*20*). However, the functional contribution of these organelles to the process of membrane fission remains unclear. We now add a further layer of complexity by identifying a key role for Arf1 and PI(4)KIIIβ on Golgi vesicles in driving late steps of mitochondrial division. These data reveal a four-way contact among mitochondria, ER, TGN, and lysosomal vesicles occurring at >80% of fission sites. It is unclear why so many organelles are required to drive mitochondrial division. In considering the contribution of PI(4)P-enriched vesicles (*24*), we envision a potential role in the recruitment of adaptors that drive Arp2/3-dependent actin polymerization at transient and localized microdomains that could allow the dynamic assembly of force-generating machineries essential for the final steps of mitochondrial division (*25*–*27*). We now suggest that the intimate contacts between mitochondria and Golgi-derived PI(4)P-containing vesicles are key modulators of mitochondrial dynamics.

REFERENCES AND NOTES

1. J. R. Friedman *et al*., *Science* **334**, 358–362 (2011).
2. E. Smirnova, L. Griparic, D. L. Shurland, A. M. van der Bliek, *Mol. Biol. Cell* **12**, 2245–2256 (2001).
3. J. E. Lee, L. M. Westrate, H. Wu, C. Page, G. K. Voeltz, *Nature* **540**, 139–143 (2016).
4. S. C. Kamerkar, F. Kraus, A. J. Sharpe, T. J. Pucadyil, M. T. Ryan, *Nat. Commun.* **9**, 5239 (2018).
5. T. B. Fonseca, Á. Sánchez-Guerrero, I. Milosevic, N. Raimundo, *Nature* **570**, E34–E42 (2019).
6. L. Tilokani, S. Nagashima, V. Paupe, J. Prudent, *Essays Biochem.* **62**, 341–360 (2018).
7. K. B. Ackema *et al*., *EMBO J.* **33**, 2659–2675 (2014).
8. A. Godi *et al*., *Nat. Cell Biol.* **1**, 280–287 (1999).
9. B. Mesmin *et al*., *Cell* **155**, 830–843 (2013).
10. J. Moser von Filseck *et al*., *Science* **349**, 432–436 (2015).
11. J. Moser von Filseck, S. Vanni, B. Mesmin, B. Antonny, G. Drin, *Nat. Commun.* **6**, 6671 (2015).
12. J. Chung *et al*., *Science* **349**, 428–432 (2015).
13. J. H. Pogson *et al*., *PLOS Genet.* **10**, e1004815 (2014).
14. G. H. Patterson, J. Lippincott-Schwartz, *Science* **297**, 1873–1877 (2002).
15. X. H. Zhao, T. Bondeva, T. Balla, *J. Biol. Chem.* **275**, 14642–14648 (2000).
16. E. Braschi, R. Zunino, H. M. McBride, *EMBO Rep.* **10**, 748–754 (2009).
17. D. Tondera *et al*., *EMBO J.* **28**, 1589–1600 (2009).
18. X. Li, S. J. Gould, *J. Biol. Chem.* **278**, 17012–17020 (2003).
19. A. Koch *et al*., *J. Biol. Chem.* **278**, 8597–8605 (2003).
20. Y. C. Wong, D. Ysselstein, D. Krainc, *Nature* **554**, 382–386 (2018).
21. S. Dowler *et al*., *Biochem. J.* **351**, 19–31 (2000).
22. G. R. Hammond, M. P. Machner, T. Balla, *J. Cell Biol.* **205**, 113–126 (2014).
23. F. Korobova, V. Ramabhadran, H. N. Higgs, *Science* **339**, 464–467 (2013).
24. R. Dong *et al*., *Cell* **166**, 408–423 (2016).
25. E. Derivery *et al*., *Dev. Cell* **17**, 712–723 (2009).
26. S. Li *et al*., *J. Cell Biol.* **208**, 109–123 (2015).
27. N. H. Hong, A. Qi, A. M. Weaver, *J. Cell Biol.* **210**, 753–769 (2015).
28. H. Lochmüller, T. Johns, E. A. Shoubridge, *Exp. Cell Res.* **248**, 186–193 (1999).
29. R. Zunino, A. Schauss, P. Rippstein, M. Andrade-Navarro, H. M. McBride, *J. Cell Sci.* **120**, 1178–1188 (2007).
30. E. Braschi *et al*., *Curr. Biol.* **20**, 1310–1315 (2010).
31. R. N. Day, M. W. Davidson, *Chem. Soc. Rev.* **38**, 2887–2921 (2009).
32. D. S. Bindels *et al*., *Nat. Methods* **14**, 53–56 (2017).
33. J. Chun, Z. Shapovalova, S. Y. Dejgaard, J. F. Presley, P. Melançon, *Mol. Biol. Cell* **19**, 3488–3500 (2008).
34. A. Sugiura, S. Mattie, J. Prudent, H. M. McBride, *Nature* **542**, 251–254 (2017).
35. J. Prudent *et al*., *Mol. Cell* **59**, 941–955 (2015).
36. J. Schindelin *et al*., *Nat. Methods* **9**, 676–682 (2012).
37. A. S. Moore, Y. C. Wong, C. L. Simpson, E. L. Holzbaur, G. K. Voeltz, *Nat. Commun.* **7**, 12886 (2016).
38. I. Arganda-Carreras, R. Fernández-González, A. Muñoz-Barrutia, C. Ortiz-De-Solorzano, *Microsc. Res. Tech.* **73**, 1019–1029 (2010).
39. C. D. Williamson, D. S. Wong, P. Bozidis, A. Zhang, A. M. Colberg-Poley, *Curr. Protoc. Cell Biol.* **68**, 3.27.1–3.27.33 (2015).

ACKNOWLEDGMENTS

We thank S. Mattie for contributions to TEM sample preparation and image acquisition. **Funding:** This work was supported by the Canadian Institutes of Health Research Operating Grants Program (CIHR grant 68833 to H.M.M.), the Medical Research Council (MRC grants MC_UU_00015/7 and RG89175 to J.P.), the Isaac Newton Trust (grant RG89529 to J.P.), and the Wellcome Trust Institutional Strategic Support Fund (grant RG89305 to J.P.). H.M.M. is a Canada Research Chair. S.N. and L.-C.T. are recipients of Daiichi Sankyo Foundation of Life Science and Ramon Areces postdoctoral fellowships, respectively. L.T. was supported by an MRC-funded graduate student fellowship. V.P was supported by the European Union's Horizon 2020 research and innovation program (MITODYN-749926). **Authors contributions:** S.N. performed the experiments; L.-C.T. and L.T. contributed to quantitative confocal imaging and immunoblots analysis; V.P. performed organelle fractionation; H.A. provided technical assistance; J.H.P. contributed intellectually to the initial development of the project; R.Z. contributed to biochemical analysis; H.M.M. and J.P. conceived the study, designed the experiments, and wrote the manuscript. **Competing interests:** The authors declare no competing interests. **Data and materials availability:** All data are available in the main text or the supplementary materials.

SUPPLEMENTARY MATERIALS

science.sciencemag.org/content/367/6484/1366/suppl/DC1
Materials and Methods
Table S1
Figs. S1 to S15
Movies S1 to S16
References (*28*–39)

View/request a protocol for this paper from *Bio-protocol*.

9 April 2019; resubmitted 9 December 2019
Accepted 27 February 2020
10.1126/science.aax6089

Golgi-derived PI(4)P-containing vesicles drive late steps of mitochondrial division

Shun Nagashima, Luis-Carlos Tábara, Lisa Tilokani, Vincent Paupe, Hanish Anand, Joe H. Pogson, Rodolfo Zunino, Heidi M. McBride and Julien Prudent

Science **367** (6484), 1366-1371.
DOI: 10.1126/science.aax6089

PI(4)P regulates mitochondrial fission

Mitochondria are dynamic intracellular organelles, the shape and number of which are regulated by various cell-signaling pathways. Mitochondrial division is driven by the recruitment of a constricting guanosine triphosphatase protein at sites of contact with the endoplasmic reticulum, but other factors, including lysosomes, are also involved. Nagashima *et al.* now document an essential role for Golgi-derived vesicles bearing a specific lipid—phosphatidylinositol 4-phosphate, or PI(4)P—in the final steps of mitochondrial division. Disruption of PI(4)P production results in mitochondrial morphological defects indicative of an inability to complete fission.

Science, this issue p. 1366

Science (print ISSN 0036-8075; online ISSN 1095-9203) is published by the American Association for the Advancement of Science, 1200 New York Avenue NW, Washington, DC 20005. The title *Science* is a registered trademark of AAAS.